MNRAS **000**, 1–9 (2021) Preprint 22 April 2021 Compiled using MNRAS LATEX style file v3.0

Relations between the asteroseismic indices and stellar parameters of δ Scuti stars for two years of TESS Mission

A. Hasanzadeh[1]*, H. Safari[1]†,H. Ghasemi[2]

[1]*Department of Physics, Faculty of Science, University of Zanjan, P.O. Box 45195-313, Zanjan, Iran*
[2]*Department of Physics, Institute for Advanced Studies in Basic Sciences (IASBS), Zanjan 45137-66731, Iran*

Accepted XXX. Received YYY; in original form ZZZ

ABSTRACT

We investigate the relationship between the asteroseismic indices and the physical quantities of 438 δ Scuti (DSCT) stars observed by the Transiting Exoplanet Survey Satellite (TESS) mission at 26 sectors. We study the scaling relations of stellar parameters (effective temperature, surface gravity, density, etc.) and asteroseismic indices such as fundamental frequency, large frequency separation ($\Delta\nu$), frequency of the highest peak in the spectrum, and peak of the envelope of oscillation mode ($\nu_{\rm max}$), for DSCT targets. Using an empirical relation and a two-dimensional autocorrelation method, we determine the large frequency separation for targets. We obtain a highly positive correlation between the fundamental radial pressure mode and the large separation for one-third of targets. We find a scaling relation between the large separation and $\nu_{\rm max}$ as $\Delta\nu = 0.49\nu_{\rm max}^{0.68}$, which is similar to that of the solar-like and red giant stars. We show a strong positive correlation between the effective temperature and $\nu_{\rm max}$ (Pearson correlation R=0.65); however, we obtain a very strong positive correlation (R=0.86) between $\nu_{\rm max}$ and the effective temperature multiplying by the surface gravity.

Key words: asteroseismology – techniques: photometric: TESS stars: variables: δ Scuti

1 INTRODUCTION

Asteroseismology is a useful task to diagnose the physical structure of pulsating stars (Brown & Gilliland 1994; Dupret et al. 2004b; Aerts et al. 2010; Catelan & Smith 2015; García & Ballot 2019). Due to high-resolution data received by several missions (such as the Microvariablity and Oscillations of Stars (Walker et al. 2003), Convection, Rotation and planetary Transits (Auvergne et al. 2009), and Kepler (Koch et al. 2010; Gilliland et al. 2010)) the asteroseismology methods have been widely investigated (Hon et al. 2018, 2019; Du et al. 2021). Recently, TESS provides high-quality photometric lightcurves of nearby stars (Campante et al. 2016; Huber et al. 2019). TESS surveys the most (about 85 percent) sky within the 26 sectors during two years of the primary mission (Ricker et al. 2015).

In the Hertzsprung-Russell (HR) diagram, DSCT stars with masses between 1.5 and 2.5$M_\odot$ are classified in variable stars (Breger 2000a; Antoci et al. 2019). They mostly show p modes with frequencies in the range of 5–80 cycles per day (d^{-1}), which may be excited by the κ mechanism (Breger 2000b; Dupret et al. 2004a; Balona 2014; Xiong et al. 2016). The effective temperature of DSCT stars is in the range of 6000 to 9000 Kelvin, which is classified as late A to F stars (Uytterhoeven et al. 2011). Some of the DSCT stars show the gravity modes in their spectrum that classified as hybrid stars (Balona & Dziembowski 2011; Bradley et al. 2015). Based on the Kepler observations, Bowman & Kurtz (2018) showed that about 25 percent of the DSCT stars are hybrid variables. The hybrid oscillating stars represent both *p*– and gravity modes, which enable us to study the stellar envelopes and cores (Grigahcène et al. 2010). Murphy et al. (2019) showed that no more than 70 percent of stars in the DSCT strip pulsate, which is not well understood, yet.

Scaling relations between the asteroseismic indices and global stellar quantities were allowed to estimate the stellar parameters (Brown et al. 1991; Kallinger et al. 2010; Coelho et al. 2015; Rodrigues et al. 2017; Hekker 2020). Validation of the scaling relations is very important in asteroseismology (Huber et al. 2017; Bellinger 2019). Theoretical modeling showed that the large separation depends on the stellar density's square root (Kjeldsen & Bedding 1995; Aerts et al. 2010). So, measuring the large separation with considerable accuracy is critical in the asteroseismic analysis of pulsating stars (García Hernández et al. 2015). Suárez et al. (2014) found a relationship between the large separation and the stellar density of the DSCT stars. García Hernández et al. (2015, 2017) used the characteristics of binaries with a δ Scuti component to determine a relationship for the stellar density and large separation, which was slightly deviated from the theoretical relation. Bedding et al. (2020) modified the theoretical relation for the large sepa-

* E-mail: hasanzadeh@znu.ac.ir † E-mail: safari@znu.ac.ir

ration of 60 DSCT stars, which approximately equals 0.85 of the theoretical value. Furthermore, Stello et al. (2009) showed that the large separation is correlated with the maximum power frequency for solar-like stars. The relation between the effective temperature and frequencies of stars is another critical issue in asteroseismology (Barceló Forteza et al. 2020). Bowman & Kurtz (2018) showed that the effective temperature of DSCT stars is positively correlated with the mode's frequency with the highest-peak amplitude.

Here, we used the TESS data to study the asteroseismic properties of 438 DSCT candidates. To do this, we apply several frequency analysis packages to obtain the oscillation spectrum of stars. Also, we collect the stellar parameters of these stars from the latest TESS catalogue. The relationship between the asteroseismic indices and stellar quantities is investigated.

Section 2 gives the data for DSCT stars. Section 3 introduces the lightcurves and asteroseismic analysis. Sections 4 and 5 represent the results and conclusion, respectively.

2 DATA

NASA's TESS mission launched in April 2018. TESS is a high-precision photometric instrument and developed to monitor stars to find exoplanets via transit methods (Sullivan et al. 2015; Barclay et al. 2018).

The TESS primary mission surveyed the sky in 26 sectors for more than several million stars in a red filter of approximately 600-1000 nm (Silva Aguirre et al. 2015). TESS observed each sector for 27 days (Barclay et al. 2018). TESS also observed around 200,000 stars with a cadence of 2 minutes (Campante et al. 2016; Stassun et al. 2018; Feinstein et al. 2019). Characterization of stars through asteroseismology allows determining the properties of their interiors (Huber et al. 2013; Silva Aguirre et al. 2015). TESS data collected from MAST[1] in both target pixels (TPFs) and lightcurve (LC) files. We used LC files that calibrated by Pre-search Data Conditioning Simple Aperture Photometry (PDCSAP) (Jenkins et al. 2016). We selected about 4000 targets from TESS Asteroseismic Science Consortium (TASC)-WG4 (AF-stars)[2] list. We checked our DSCT star candidates with Kepler's catalogue (Bradley et al. 2015; Uytterhoeven et al. 2011; Bowman & Kurtz 2018). Also, we checked out the regular frequency spacing (echelle diagram) in their pulsation spectra (Section 3.2) as an additional criterion for selecting the targets. Our goal is to analyse the DSCT stars with many frequencies, so we limited our list by removing stars with a single (or double) frequency from the analysis. So, considering the above criteria, the final list is reduced to 438 Scuti stars. We analysed the short cadence (2 min) PDCSAP lightcurve of 438 DSCT stars for two years of observation in sectors 1 to 26.

We used the latest TESS catalogue (Stassun et al. 2019) to extract the positions, magnitudes, and stellar parameters (such as effective temperature, mass, surface gravity, stellar density, and luminosity) for DSCT stars. Figure 1 shows the position of 438 stars in the celestial sphere.

[1] https://archive.stsci.edu [2] https://tasoc.dk/wg4

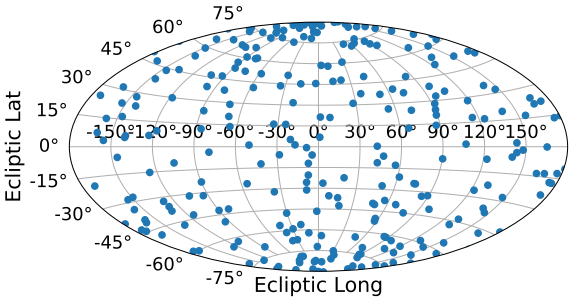

Figure 1. Position (Ecliptic latitude and longitude) of 438 DSCT stars (blue dots) in the celestial sphere were detected from July 2018 to July 2020.

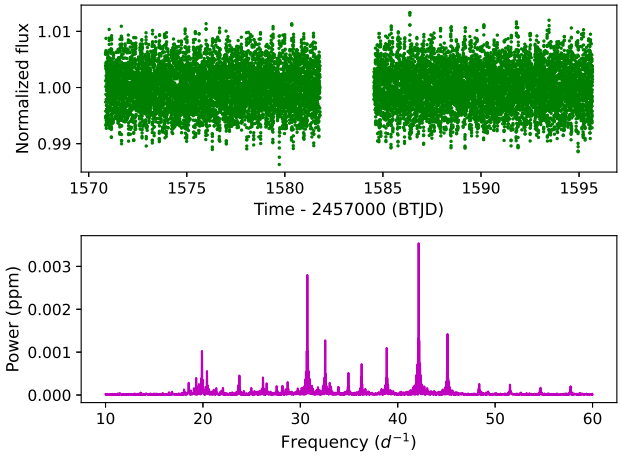

Figure 2. Upper panel: LC of TIC9591460 recorded by TESS during sector 10. Lower panel: The Lomb–Scargle periodogram represents the amplitude (in ppm units) versus the frequency (d^{-1})

3 METHODS

3.1 Lightcurve analysis

We analysed the frequency modes of 438 selected DSCT stars. To do this, first, we removed 4σ outlier data points from the PDCSAP LC of each star. Then, the resultant are smoothed (Savitzky & Golay 1964) and normalised to their average intensity. Figure 2 represents a sample LC of TIC9591460. Changing the size of aperture pixel file for each star (Fig. 3) is a standard way to increase the accuracy. For too small aperture TPF, increasing the aperture size for a target allows capturing extra flux. Also, decreasing the aperture's size may remove the contamination effects from nearby objects and increase the signal-to-noise ratio (SNR) (Lund et al. 2017; Marchiori et al. 2019). We made a LC for each case from TPF to compare with the PDCSAP LC and improve the SNR. We applied a standard Lomb-Scargle periodogram via the Lightkurve package (Lightkurve Collaboration et al. 2018) to extract the frequency of oscillations of DSCT stars. Lightkurve is an open-source to study the photometric data for TESS observations. This package provides the asteroseismic power spectra and oscillation modes. In

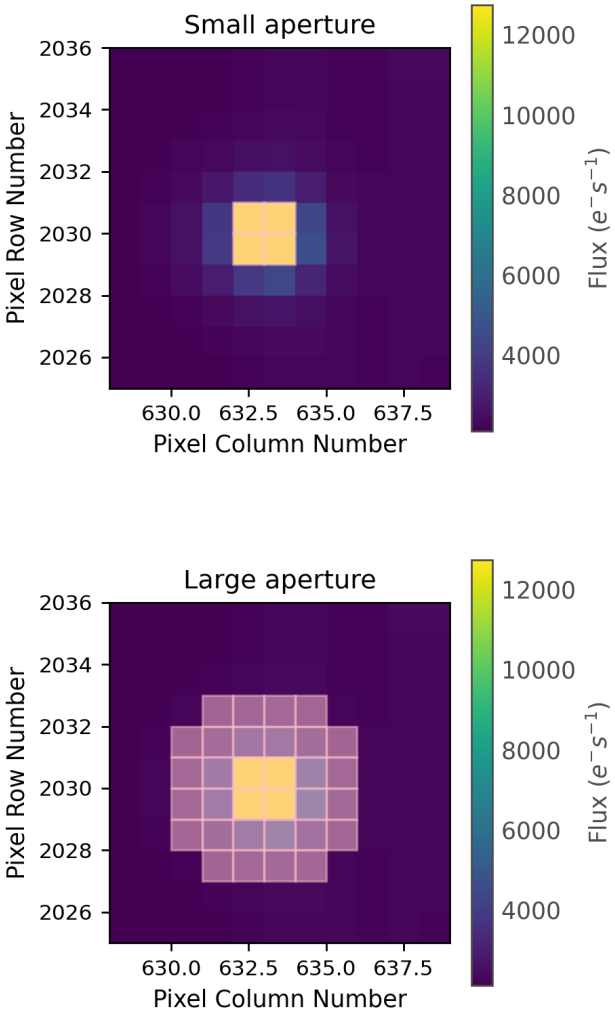

Figure 3. Pixel file image of TIC9591460 star for the small (top) and large (bottom) apertures (mask).

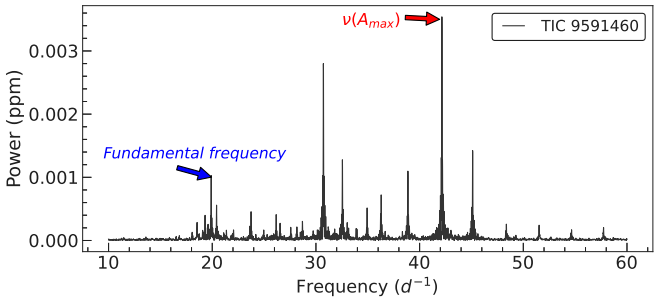

Figure 4. Fundamental frequency (blue arrow) and $\nu(A_{\max})$ (red arrow) for TIC9591460.

the analysis, we considered the frequencies with an SNR of more than 4. To ensure the validity of frequencies, we also applied other standard frequency analysis codes (KU Leuven pipeline: (Degroote et al. 2009); SMURFS: (Müllner 2020)). The KU Leuven iterative pre-whitening pipeline uses the Lomb-Scargle periodogram and optimization method to find the power spectrum (Pápics et al. 2012; Van Reeth et al. 2015). SMURFS developed to obtain frequencies of LC from TESS observations. This code computes the possible frequency combinations instead of the pre-whitening method.

3.2 Asteroseismic analysis

In asteroseismology, a star's basic information can be deduced from the seismic indices. The relations between the global seismic indices (frequency of the highest-peak amplitude, fundamental frequency, large frequency separation, etc.) and stellar characteristics (mass, gravity, temperature, radius, etc.) have been widely developed (Coelho et al. 2015; Yu et al. 2018; Barceló Forteza et al. 2020). Oscillations of a star interpret via a superposition of the radial wave functions and spherical harmonics. Each mode indicates the radial number (n), angular degree (l), and azimuthal order (m), which show properties of the oscillations. The fundamental radial mode defines with the radial number $n = 1$ and angular number $l = 0$ that usually expected to appear for the highest-peak amplitude if it is excited (Aerts et al. 2010; Murphy et al. 2020). However, the previous study (Bedding et al. 2020) on the DSCT stars showed that the fundamental radial modes did not often appear the highest-peak amplitudes in the power spectrum (see also Murphy et al. (2020)). We applied the following criteria to identify the fundamental mode of oscillations for our targets. The lowest frequency with a strong amplitude (with amplitude usually 0.2 greater than highest-peak to ensure that the mode is above the noise level as well as an SNR of more than four (Fig. 4)) and satisfied the period-luminosity relation. Studies (Breger & Bregman 1975; McNamara 2011) showed that the DSCT stars follow a relation between the pulsation period (P) and the luminosity. Ziaali et al. (2019) obtained a relation for period-luminosity as $M_V = (-2.94 \pm 0.06) \log P(\text{day}) - (1.34 \pm 0.06)$ in which M_V is the absolute visible magnitude. Our analysis shows that about one-third of samples (142 targets) obey the above criteria, which is in good agreement with Bedding et al. (2020).

For the power spectrum of each DSCT star, the frequency related to the highest-peak amplitude is called $\nu(A_{\max})$. It is well-known that due to amplitude modulation mechanisms and noise background (Bowman 2017), the $\nu(A_{\max})$ may be changed with time. Therefore, it was suggested to use the frequency of the envelope's peak ($\nu_{\max}$) instead of $\nu(A_{\max})$ in an SNR periodogram. To generate the SNR periodogram, we divided the power by the noise spectrum. Applying an autocorrelation method (Mosser & Appourchaux 2009), we determined $\nu_{\max}$ (Fig. 5). The method investigated for autocorrelations on several windows of the frequency spectrum to obtain the frequency range for the modes' envelope. To do this, first, we reduced the background from the smoothed spectrum. Second, we applied the autocorrelation for a window of the background smoothed spectrum. Third, a Gaussian curve is fitted to the mean collapsed correlation within each window. Finally, we determined the frequency ($\nu_{\max}$) of peak in the Gaussian fitted curve. Viani et al. (2019) gave the details of the method to determine the $\nu_{\max}$.

Large frequency separation ($\Delta\nu$) is another important seismic quantity in asteroseismology. For a given angular degree (l), $\Delta\nu$ defines the average frequency spacing between consecutive radial modes (Aerts et al. 2010). To determine $\Delta\nu$, for a given $\nu_{\max}$, we considered a window with the size of one FWHM of the envelope

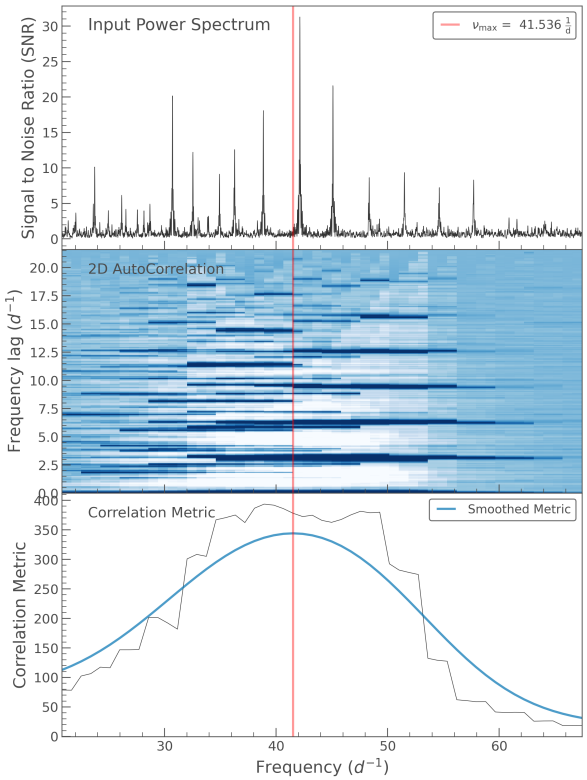

Figure 5. Upper panel: The SNR periodogram for TIC9591460. The red line indicates the $\nu_{\max}$. Middle panel: Two-dimensional autocorrelation applied to periodogram. Lower panel: The mean collapsed correlation versus central frequency (see Viani et al. (2019)), and a Gaussian smoothed curve (blue line).

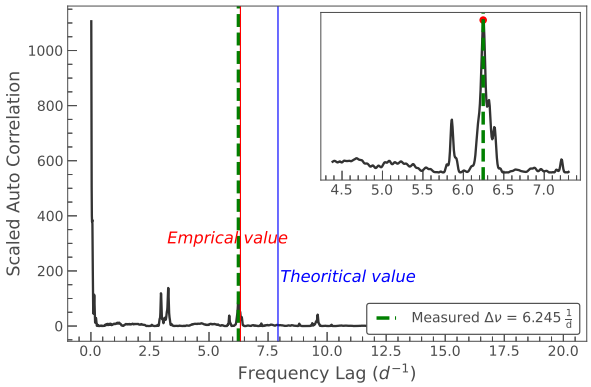

Figure 6. The large frequency separation ($\Delta\nu$) of the seismic oscillations of TIC9591460 using a 2D autocorrelation method. The theoretical ($\Delta\nu = \sqrt{\rho}$), empirical ($\Delta\nu = 0.78\rho^{0.46}$), and obtained $\Delta\nu$ based on the 2D autocorrelation method for the large frequency separation are indicated by blue, red, and dashed green lines, respectively.

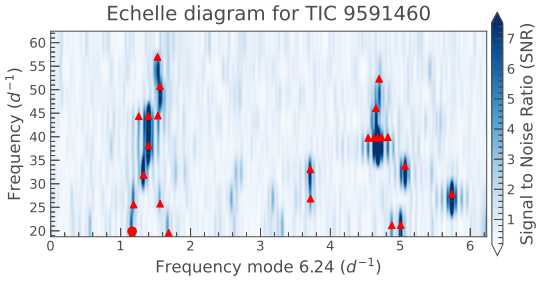

Figure 7. The echelle diagram in a colour scale for TIC9591460 with an average large frequency separation about $\Delta\nu$=6.24 d^{-1}. The circle and triangles indicate the fundamental mode and high overtone modes, respectively.

on both sides (includes all of the visible mode peaks). Then, a 2D autocorrelation method is applied to the regions around the $\nu_{\max}$. Detail of the 2D autocorrelation method was given by Viani et al. (2019). Using an automatic peak finding algorithm (Huber et al. 2009; Mosser & Appourchaux 2009) for the peaks in the vicinity of an empirical value (based on the relation between the density and $\Delta\nu$), we obtained the final value for the large frequency separation (see Fig. 6). The empirical relations between the mean density (ρ) and $\Delta\nu$ for DSCT stars were investigated by García Hernández et al. (2015); Chen et al. (2019); Rodríguez-Martín et al. (2020). In the literature (Aerts et al. 2010; Tassoul 1980; Ulrich 1986; Kjeldsen et al. 1995), for the oscillation modes with $n \gg l$ (high-order modes), a theoretical asymptotic relation between the large frequency separation and mean stellar density was investigated as $\Delta\nu \propto \sqrt{\rho}$. However, DSCT pulsations are in the non-asymptotic regime (Paparó et al. 2016; Mirouh et al. 2019), so we expect a deviation from the asymptotic relation. Suárez et al. (2014) predicted an empirical scaling relation between the large separation and stellar density as $\Delta\nu = 0.78\rho^{0.46}$. Also, based on the TESS and Kepler observations for 60 high-frequency DSCT stars, Bedding et al. (2020) obtained a relation as $\Delta\nu = 0.85\sqrt{\rho}$. We found that Bedding et al. relation stays between the theoretical and empirical scaling relations (Fig. 13). Rodríguez-Martín et al. (2020) studied the effect of rotation on the empirical relation for low-order DSCT stars.

In our analysis, we considered the large frequency separation less than 25 percent deviation from the empirical scaling relation as well as regular frequency spacings in the echelle diagram for DSCT stars. An echelle diagram (Grec et al. 1983) is a useful tool in asteroseismology to display the oscillation frequencies and mode identification. The frequency spectrum is divided into segments of $\Delta\nu$ and collects in an echelle diagram. In echelle diagram, the modes with a similar angular degree are arranged close to a vertical ridge. The considerable variations in the large frequency separation have appeared like curvature in the diagram. As expected, close to the vertical ridges have corresponded to the correct $\Delta\nu$ in the diagram (Fig. 7).

4 RESULTS

We determined the asteroseismic quantities for 438 DSCT stars observed by the TESS mission. We extracted the stellar parameters for targets from the revised TESS catalogue (Stassun et al. 2019). TESS catalogue determines the stellar parameters by applying the Gaia DR2 (Gaia Collaboration et al. 2018), photometric, and spectroscopic data (such as 2MASS, LAMOST), as well as a set of empirical relations. The details were described by Stassun et al. (2019). We compared temperatures (all targets) and radii (286 available targets) extracted from TESS with Gaia DR2 catalogues (Fig. 8(A)&(B)). We obtained the Pearson correlation about 0.82 and 0.99 for temperatures and radii, respectively between TESS and Gaia catalogue. Therefore, we found that the temperature and radius for TESS and Gaia are in good agreement. We also compared the temperature extracted from TESS catalogue with the spectral energy distribution (SED) model for some of targets (Stassun et al. 2017; Deacon et al. 2019). For a sample of 43 stars (collected by Antoci et al. (2019)), We found the Pearson correlation about 0.74 for temperatures between the TESS catalogue and SED model (Fig. 8(C)).

Here, we studied statistical analysis and scaling relations for asteroseismic and stellar parameters of DSCT stars. Figure 9 represents the frequency distribution of mass, radius, effective temperature, and surface gravity for 438 Scuti stars. The mass, radius, effective temperature, and surface gravity for DSCT targets are in the range of 1.4 to 2.4$M_{\odot}$, 1.3 to 4.8$R_{\odot}$, 6600 to 9400 K, and 3.3 to 4.5 dex, respectively. As shown in the figure, mass and effective temperature values agree with the previous reports for DSCT stars (Daszyńska-Daszkiewicz 2007; Antoci et al. 2019). Table 1 represents the asteroseismic indices and stellar parameters for a sample of 50 DSCT stars. A supplement to this paper provides the electronic table contains the sector number, positions, asteroseismic indices, and stellar quantities for 438 DSCT stars.

We applied the maximum likelihood method to estimate the fitting parameters via a numerical optimization technique. Also, we used the Markov chain Monte Carlo (MCMC) approach to investigate the uncertainties in the observations propagated into the fit parameters (Goodman & Weare 2010). A brief discussion of MCMC and detail of codes were given by Foreman-Mackey et al. (2013).

Figure 10 shows the histogram (frequency-size distribution) of the large frequency separation and fundamental mode for 438 and 142 (about one-third of our targets), respectively. The large frequency separation and fundamental frequency are in the range of 1.27 to 7.86 d^{-1} and 6.0 to 26.8 d^{-1}, respectively. Also, the peak of distribution for the fundamental frequency as well as the large frequency separation is in the range of 12 to 23 d^{-1} and 6 to 7 d^{-1}, respectively.

The scatter plot of $\nu(A_{\max})$ via $\nu_{\max}$ is shown in Fig. 11. We see that $\nu(A_{\max})$ is highly correlated (correlation coefficient R=0.92) with $\nu_{\max}$ for DSCT stars. Since, the frequency with the highest-peak may change with time (Fig. 12), so we used $\nu_{\max}$ instead of the highest-peak in our further analysis.

Figure 13 depicts the relation between the large separation and stellar density for DSCT stars. A power function $\Delta\nu = (0.76 \pm 0.01)\rho^{(0.43\pm0.02)}$ is fitted to data. As we observed in the figure, the fitted relation slightly deviated from the theoretical and empirical relations (Suárez et al. 2014; Bedding et al. 2020).

Figure 14 shows the relation between the $\nu_{\max}$ and effective temperature of 438 targets. We observed a strong positive correlation (correlation coefficient R=0.65) between the $\nu_{\max}$ and $T_{\rm eff}$, which is recognized with the surface gravity in the colour plot (Fig. 14 upper panel). As well, a straight line with the marginalization of parameters due to uncertainties of observations via the MCMC method is fitted as $T_{\rm eff} = (1.14 \pm 0.07)\nu_{\max}+(1.22 \pm 0.01)$. Barceló Forteza et al. (2018) showed that the effective temperature is correlated with $\nu_{\max}$. Figure 14 (lower panel) shows a very strong positive correlation (R=0.86) between $gT_{\rm eff}$ (the effective temperature multiplying by the mean surface gravity) and $\nu_{\max}$. Also, this positive correlation is presented by a fitted straight line ($gT_{\rm eff} = (7.16 \pm 0.19)\nu_{\max}+(0.11 \pm 0.02)$). Bowman & Kurtz (2018) showed that the scaling relation for effective temperature is differentiated for various evolutionary stages that indicated by surface gravity. According to Bowman & Kurtz (2018) (Figure 3 therein) and Barceló Forteza et al. (2020) (Figure 6 therein), the surface gravity decreases with increasing the temperature for a constant highest-peak frequency or envelope's peak frequency.

Figure 15 illustrates the relationship between the fundamental frequency (ν_f) and large frequency separation for 142 Scuti stars, which satisfied the well-known relation between the period and luminosity. The fundamental frequency and large frequency separation for these stars satisfy a positive correlation ($\nu_f = (2.78 \pm 0.28)\Delta\nu + (1.66 \pm 1.53)$). We obtained a power relation ($\Delta\nu = (0.49 \pm 0.12)\nu_{\max}^{(0.68\pm0.07)}$) between $\Delta\nu$ and $\nu_{\max}$ for 438 DSCT stars (Fig. 16). To do this, a power-law model is fitted to binned data based on the maximum likelihood method and MCMC approach. Similar power-law behavior for solar-like (Stello et al. 2009; Huber et al. 2011) and red giant stars (Yu et al. 2018) with index in the range of 0.7 to 0.8 were investigated. The stars classify in three groups with different surface gravity $3 \leqslant \log g \leqslant 3.5$, $3.5 < \log g \leqslant 4.0$, and $4.0 < \log g \leqslant 4.5$, which is related to the Terminal-age main sequence (TAMS), Mid-age main sequence (MAMS), and zero-age main sequence (ZAMS) stars, respectively (Bowman & Kurtz 2018).

5 CONCLUSION

We applied the frequency analysis to find the asteroseismic indices of 438 DSCT stars observed by TESS mission. We obtained the high-frequency limit about 80 d^{-1} for our samples, which is verified the previous studies (Breger 2000b; Bowman & Kurtz 2018). We validated the stellar parameters by Gaia catalogue and SED model. The main results of this paper are summarised as follows:

- We obtained the fundamental frequencies (ν_f) in the range of 6.0 to 26.8 d^{-1} for 142 targets. Among 142 targets, for 35 (about 25 percent) of stars, the fundamental frequencies are same (or very close) to the highest-peak amplitudes, but for the remaining stars, ν_fs depart from the frequency of highest peak. It seems that the peak value of amplitudes is sensitive to the line of sight or instrument (Lignières & Georgeot 2009). For example, as we observed in the power spectrum (sectors 2 and 3) for TIC66434034 star (Fig. 12), the frequency with the highest power changes with time (Handler et al. 1998; Breger 2000b; Barceló Forteza et al. 2015). Another reason for changing the amplitude of frequencies may be related to the long-term variability behaviour (Arentoft et al. 2001), and frequency phase modulation of DSCT stars (Bowman et al. 2016; Khalack et al. 2019). Numerical modeling via the stellar oscillation codes (e.g., GYRE) may be accurately address the physical mechanisms behind the amplitude variation of frequencies on DSCT stars.
- We determined the fundamental frequency for about one-third targets (142 cases), which is agreement with Bedding et al. (2020).

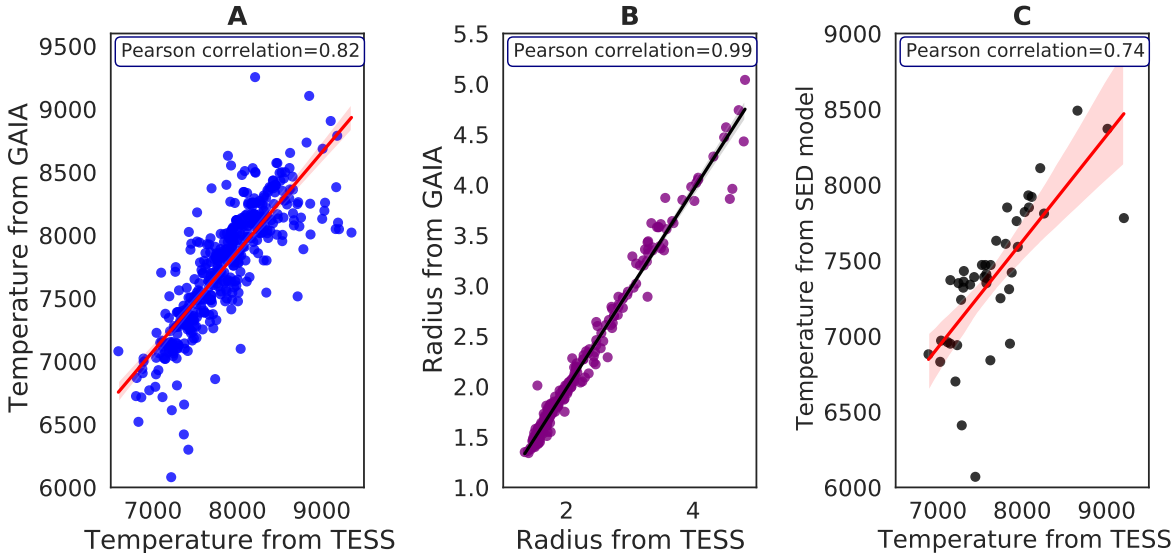

Figure 8. Comparison of the temperature for DSCT stars extracted from TESS and Gaia DR2 catalogues (panel A), radius extracted from TESS and Gaia DR2 catalogues (panel B), and temperature extracted from TESS catalogue and SED model (panel C). Temperature and radius are measured in kelvin and solar unit, respectively.

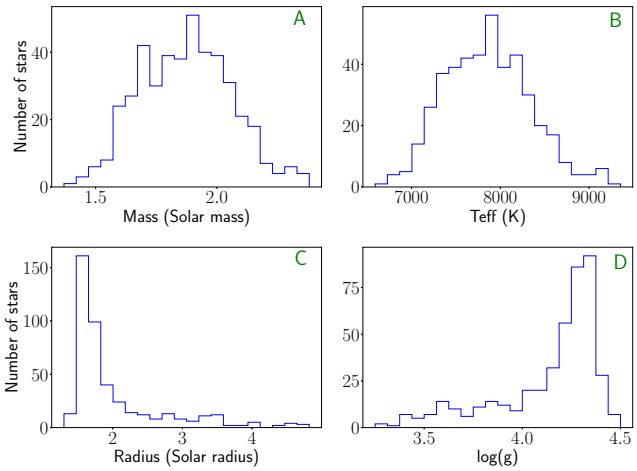

Figure 9. Frequency distribution of the mass (A), radius (B), effective temperature (C), and surface gravity (D) for 438 DSCT stars.

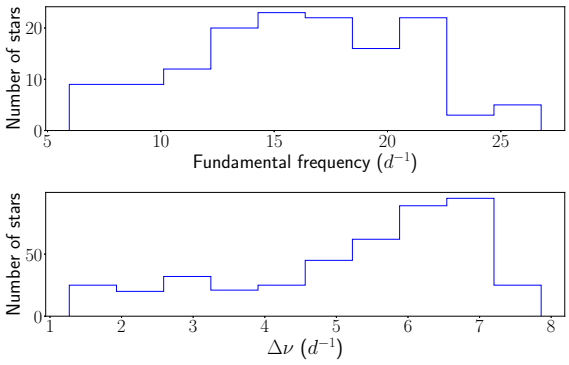

Figure 10. Frequency distribution of the fundamental mode (d^{-1}) and large separation (d^{-1}) for 142 and 438 DSCT stars, respectively.

We found a linear relation as $\nu_f = (2.78 \pm 0.28)\Delta\nu + (1.66 \pm 1.53)$ for the fundamental frequency and large frequency separation.

- We modified a relation between the large frequency separation and stellar density as $\Delta\nu = (0.76 \pm 0.01)\rho^{0.43\pm0.02}$ for DSCT stars (Fig. 13), which is slightly deviated from the theoretical and empirical relations (Suárez et al. 2014; Bedding et al. 2020). This asteroseismic relation can help us calculate the mean stellar density of individual DSCT star by analysing the photometric lightcurves (Huber et al. 2019).

- We obtained a positive correlation between the $\Delta\nu$ and $\nu_{\rm max}$ as $\Delta\nu = (0.49 \pm 0.12)\nu_{\rm max}^{(0.68\pm0.07)}$ for Scuti stars (Fig. 16). We found that the DSCT stars are classified into three groups with surface gravity $3 \leqslant \log g \leqslant 3.5$, $3.5 < \log g \leqslant 4.0$, and $4.0 < \log g \leqslant 4.5$, which is related to the TAMS, MAMS, and ZAMS stars, respectively. This classification of stars in different groups via the surface gravity can be considered an indicator in their evolutionary stages (Bowman & Kurtz 2018; Barceló Forteza et al. 2020).

- We obtained a strong positive correlation (R=0.65) between the envelope's peak of oscillation modes and effective temperature of 438 targets (Fig. 14 upper panel), which is in good agreement with previous studies (Breger 2000b; Huber et al. 2011; Barceló Forteza et al. 2018; Bowman & Kurtz 2018; Barceló Forteza et al. 2020).

- We observed a positive correlation (R=0.86) between the envelope's peak and $gT_{\rm eff}$ (Fig. 14 lower panel) for our DSCT targets. Christensen-Dalsgaard (2000) suggested that old stars (stars with

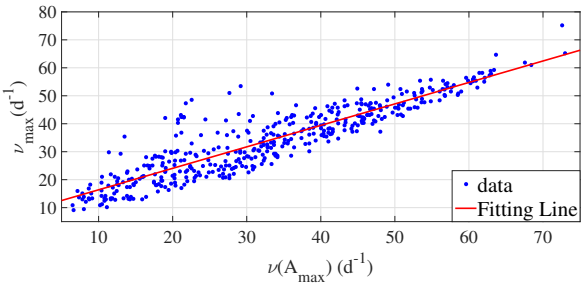

Figure 11. Scatter plot of $\nu_{\max}$ versus $\nu(A_{\max})$. $\nu_{\max}$ shows a linear relation as $\nu_{\max} = (0.77 \pm 0.03)\nu(A_{\max})+(8.58 \pm 1.21)$ and highly correlation (Pearson correlation about 0.91) with $\nu(A_{\max})$.

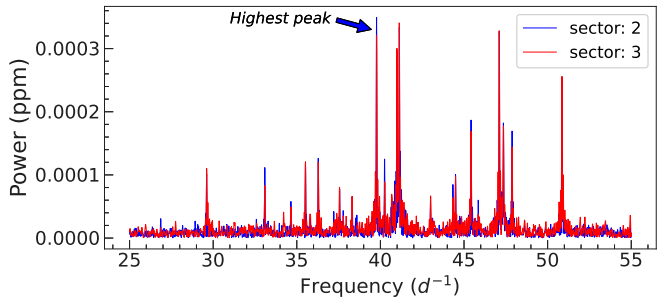

Figure 12. The Frequency power spectrum of TIC66434034 star observed in sector 2 (blue line) and 3 (red line). The frequency of the highest-peak (blue arrow) changes with time.

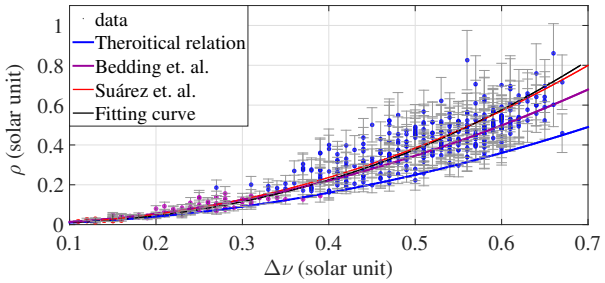

Figure 13. The mean stellar density (ρ) versus large frequency separation ($\Delta\nu$) for 438 DSCT stars, which are recognised with $3 \leqslant \log g \leqslant 3.5$ (red circles), $3.5 < \log g \leqslant 4.0$ (purple circles), and $4.0 < \log g \leqslant 4.5$ (blue circles). The fitted curve $\Delta\nu = (0.76 \pm 0.01)\rho^{0.43\pm0.02}$ presented by black line. The theoretical (blue line) $\Delta\nu = \sqrt{\rho}$ (Aerts et al. 2010), empirical relations $\Delta\nu = 0.78\rho^{0.46}$ (red line), and $\Delta\nu = 0.85\sqrt{\rho}$ (purple line) are introduced by Suárez et al. (2014) and Bedding et al. (2020), respectively.

lower surface gravity) have lower frequencies. Recent studies (Bowman & Kurtz 2018; Barceló Forteza et al. 2020) investigated that the surface gravity decreases with increasing the temperature for a constant characteristic frequency (highest-peak or envelope's peak frequency) of DSCT stars. However, previous studies (Brown et al. 1991; Kjeldsen & Bedding 1995; Chaplin & Miglio 2013) obtained a scaling relation ($\nu_{\max} \propto g/\sqrt{T_{\rm eff}}$) for solar like and red giant stars.

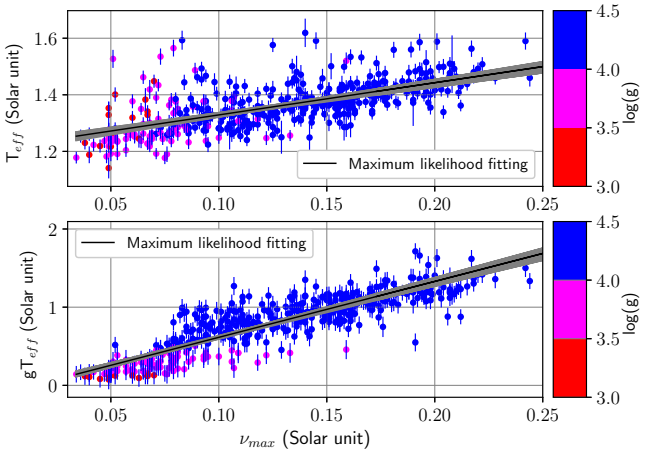

Figure 14. Upper panel: Relation between the $\nu_{\max}$ and effective temperature. The correlation coefficient is obtained about R=0.65. Lower panel: Relation between the $\nu_{\max}$ and effective temperature multiplying by surface gravity ($gT_{\rm eff}$). The correlation coefficient is obtained about R=0.86. The DSCT stars classify into three groups with different surface gravity, as explained in Figure 13.

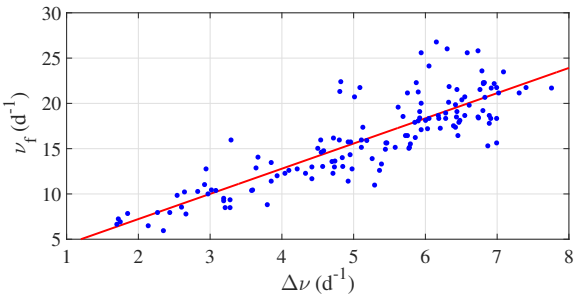

Figure 15. Scatter plot of the large frequency separation versus the fundamental frequency for 142 DSCT stars. We fitted a linear line as $\nu_f = (2.78 \pm 0.28)\Delta\nu + (1.66 \pm 1.53)$ to data.

The discrepancy between the scaling relations may come from the different nature of stars. This may be described by the excitation of higher-radial modes in DSCT stars with large temperatures as expected in agreement with the frequencies for kappa-mechanism (Balona & Dziembowski 2011).

ACKNOWLEDGMENTS

This manuscript includes data collected by the TESS mission, which are publicly available from the Mikulski Archive for Space Telescopes (MAST). Funding for the TESS mission is provided by the NASA Explorer Program. Funding for the TESS Asteroseismic Science Operations Centre is provided by the Danish National Research Foundation (Grant agreement no.: DNRF106), ESA PRODEX (PEA 4000119301) and Stellar Astrophysics Centre (SAC) at Aarhus University. Authors acknowledge the effort made by TASOC WG4 that helped us in our target selection.

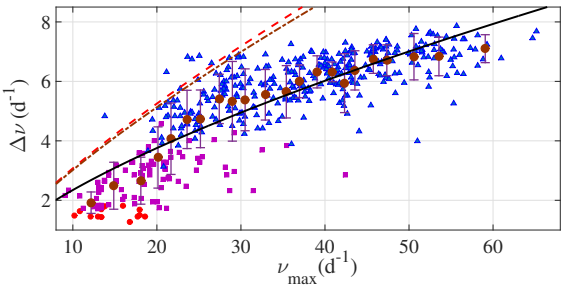

Figure 16. Scatter plot for the large frequency separation and ν_{max}. The colour of each target represents its related surface gravitation. The power-law curve (black line) $\Delta\nu = a\nu_{max}^{b}$ with a =0.49±0.12 and b =0.68±0.07 is fitted to the binned data (circle marks together with error bars). A similar power-law model for solar-like stars (brown dashed line) and red giant stars (red dash–dotted line) with arbitrary intercept are presented. The auxiliary information is given in Figure 13.

DATA AVAILABILITY

All of the TESS data used within this article are made publicly available as a supplementary table. Also, all stellar parameters presented in this paper have been extracted from TESS Input Catalogue (TIC V8) that are available from the Exoplanet Follow-up Observing Program for TESS (ExoFOP-TESS, https://exofop.ipac.caltech.edu/tess/index.php). All other data related to figures are will be shared on request to the corresponding author.

REFERENCES

Aerts C., Christensen-Dalsgaard J., Kurtz D. W., 2010, Asteroseismology. Springer

Antoci V., et al., 2019, MNRAS, 490, 4040

Arentoft T., et al., 2001, A&A, 374, 1056

Auvergne M., et al., 2009, A&A, 506, 411

Balona L. A., 2014, MNRAS, 437, 1476

Balona L. A., Dziembowski W. A., 2011, MNRAS, 417, 591

Barceló Forteza S., Michel E., Roca Cortés T., García R. A., 2015, A&A, 579, A133

Barceló Forteza S., Roca Cortés T., García R. A., 2018, A&A, 614, A46

Barceló Forteza S., Moya A., Barrado D., Solano E., Martín-Ruiz S., Suárez J. C., García Hernández A., 2020, A&A, 638, A59

Barclay T., Pepper J., Quintana E. V., 2018, ApJS, 239, 2

Bedding T. R., et al., 2020, Nature, 581, 147

Bellinger E. P., 2019, MNRAS, 486, 4612

Bowman D. M., 2017, Amplitude Modulation of Pulsation Modes in Delta Scuti Stars, doi:10.1007/978-3-319-66649-5.

Bowman D. M., Kurtz D. W., 2018, MNRAS, 476, 3169

Bowman D. M., Kurtz D. W., Breger M., Murphy S. J., Holdsworth D. L., 2016, MNRAS, 460, 1970

Bradley P. A., Guzik J. A., Miles L. F., Uytterhoeven K., Jackiewicz J., Kinemuchi K., 2015, AJ, 149, 68

Breger M., 2000a, in Breger M., Montgomery M., eds, Astronomical Society of the Pacific Conference Series Vol. 210, Delta Scuti and Related Stars. p. 3

Breger M., 2000b, MNRAS, 313, 129

Breger M., Bregman J. N., 1975, ApJ, 200, 343

Brown T. M., Gilliland R. L., 1994, ARA&A, 32, 37

Brown T. M., Gilliland R. L., Noyes R. W., Ramsey L. W., 1991, ApJ, 368, 599

Campante T. L., et al., 2016, ApJ, 830, 138

Catelan M., Smith H. A., 2015, Pulsating Stars. Wiley-VCH

Chaplin W. J., Miglio A., 2013, ARA&A, 51, 353

Chen X., Li Y., Zhang X., 2019, ApJ, 887, 253

Christensen-Dalsgaard J., 2000, in Breger M., Montgomery M., eds, Astronomical Society of the Pacific Conference Series Vol. 210, Delta Scuti and Related Stars. p. 187

Coelho H. R., Chaplin W. J., Basu S., Serenelli A., Miglio A., Reese D. R., 2015, MNRAS, 451, 3011

Daszyńska-Daszkiewicz J., 2007, Communications in Asteroseismology, 150, 32

Deacon N. R., Henning T., Kossakowski D. E., 2019, MNRAS, 486, 251

Degroote P., et al., 2009, A&A, 506, 111

Du M., Bi S., Zhang X., Li Y., Li T., Shi R., 2021, MNRAS, 501, 614

Dupret M. A., Grigahcène A., Garrido R., Gabriel M., Scuflaire R., 2004a, A&A, 414, L17

Dupret M. A., Thoul A., Scuflaire R., Daszyńska-Daszkiewicz J., Aerts C., Bourge P. O., Waelkens C., Noels A., 2004b, A&A, 415, 251

Feinstein A. D., et al., 2019, PASP, 131, 094502

Foreman-Mackey D., Hogg D. W., Lang D., Goodman J., 2013, PASP, 125, 306

Gaia Collaboration et al., 2018, A&A, 616, A1

García R. A., Ballot J., 2019, Living Reviews in Solar Physics, 16, 4

García Hernández A., Martín-Ruiz S., Monteiro M. J. P. F. G., Suárez J. C., Reese D. R., Pascual-Granado J., Garrido R., 2015, ApJ, 811, L29

García Hernández A., et al., 2017, MNRAS, 471, L140

Gilliland R. L., et al., 2010, PASP, 122, 131

Goodman J., Weare J., 2010, Communications in Applied Mathematics and Computational Science, 5, 65

Grec G., Fossat E., Pomerantz M. A., 1983, Sol. Phys., 82, 55

Grigahcène A., et al., 2010, ApJ, 713, L192

Handler G., Pamyatnykh A. A., Zima W., Sullivan D. J., Audard N., Nitta A., 1998, MNRAS, 295, 377

Hekker S., 2020, Frontiers in Astronomy and Space Sciences, 7, 3

Hon M., Stello D., Zinn J. C., 2018, ApJ, 859, 64

Hon M., Stello D., García R. A., Mathur S., Sharma S., Colman I. L., Bugnet L., 2019, MNRAS, 485, 5616

Huber D., Stello D., Bedding T. R., Chaplin W. J., Arentoft T., Quirion P. O., Kjeldsen H., 2009, Communications in Asteroseismology, 160, 74

Huber D., et al., 2011, ApJ, 743, 143

Huber D., et al., 2013, ApJ, 767, 127

Huber D., et al., 2017, ApJ, 844, 102

Huber D., et al., 2019, AJ, 157, 245

Jenkins J. M., et al., 2016, in Software and Cyberinfrastructure for Astronomy IV. p. 99133E, doi:10.1117/12.2233418

Kallinger T., et al., 2010, A&A, 522, A1

Khalack V., et al., 2019, MNRAS, 490, 2102

Kjeldsen H., Bedding T. R., 1995, A&A, 293, 87

Kjeldsen H., Bedding T. R., Viskum M., Frand sen S., 1995, AJ, 109, 1313

Koch D. G., et al., 2010, ApJ, 713, L79

Lightkurve Collaboration et al., 2018, Lightkurve: Kepler and TESS time series analysis in Python (ascl:1812.013)

Lignières F., Georgeot B., 2009, A&A, 500, 1173

Lund M. N., Handberg R., Kjeldsen H., Chaplin W. J., Christensen-Dalsgaard J., 2017, in European Physical Journal Web of Conferences. p. 01005 (arXiv:1610.02702), doi:10.1051/epjconf/201716001005

Marchiori V., et al., 2019, A&A, 627, A71

McNamara D. H., 2011, AJ, 142, 110

Mirouh G. M., Angelou G. C., Reese D. R., Costa G., 2019, MNRAS, 483, L28

Mosser B., Appourchaux T., 2009, A&A, 508, 877

Müllner M., 2020, SMURFS: Automated frequency extraction from time series data, doi:10.5281/zenodo.3635801, https://doi.org/10.5281/zenodo.3635801

Murphy S. J., Hey D., Van Reeth T., Bedding T. R., 2019, MNRAS, 485, 2380

Murphy S. J., Paunzen E., Bedding T. R., Walczak P., Huber D., 2020, MNRAS, 495, 1888

Paparó M., Benkő J. M., Hareter M., Guzik J. A., 2016, ApJS, 224, 41

Pápics P. I., et al., 2012, A&A, 542, A55
Ricker G. R., et al., 2015, Journal of Astronomical Telescopes, Instruments, and Systems, 1, 014003
Rodrigues T. S., et al., 2017, MNRAS, 467, 1433
Rodríguez-Martín J. E., García Hernández A., Suárez J. C., Rodón J. R., 2020, MNRAS, 498, 1700
Savitzky A., Golay M. J. E., 1964, Analytical Chemistry, 36, 1627
Silva Aguirre V., et al., 2015, MNRAS, 452, 2127
Stassun K. G., Collins K. A., Gaudi B. S., 2017, AJ, 153, 136
Stassun K. G., et al., 2018, AJ, 156, 102
Stassun K. G., et al., 2019, AJ, 158, 138
Stello D., Chaplin W. J., Basu S., Elsworth Y., Bedding T. R., 2009, MNRAS, 400, L80
Suárez J. C., García Hernández A., Moya A., Rodrigo C., Solano E., Garrido R., Rodón J. R., 2014, A&A, 563, A7
Sullivan P. W., et al., 2015, ApJ, 809, 77
Tassoul M., 1980, ApJS, 43, 469
Ulrich R. K., 1986, ApJ, 306, L37
Uytterhoeven K., et al., 2011, A&A, 534, A125
Van Reeth T., et al., 2015, A&A, 574, A17
Viani L. S., Basu S., Corsaro E., Ball W. H., Chaplin W. J., 2019, ApJ, 879, 33
Walker G., et al., 2003, PASP, 115, 1023
Xiong D. R., Deng L., Zhang C., Wang K., 2016, MNRAS, 457, 3163
Yu J., Huber D., Bedding T. R., Stello D., Hon M., Murphy S. J., Khanna S., 2018, ApJS, 236, 42
Ziaali E., Bedding T. R., Murphy S. J., Van Reeth T., Hey D. R., 2019, MNRAS, 486, 4348

This paper has been typeset from a TEX/LATEX file prepared by the author.

Table 1. TIC number, Sector number, positions (in RA and Dec), Effective temperature ($T_{\rm eff}$), mass ($M/M_{\odot}$), radius ($R/R_{\odot}$), surface gravity ($\log g$), luminosity ($L/L_{\odot}$), Density ($\rho/\rho_{\odot}$),TESS magnitude, fundamental frequency (ν_f), the highest-peak of spectrum ($\nu(A_{\rm max})$), the peak of the envelope of oscillation mode ($\nu_{\rm max}$), large frequency separation ($\Delta\nu$) for 438 DSCT stars.

TIC Number	Sector	Positions RA	Dec	T_{eff} (K)	Mass ($M/M_{\odot}$)	Radius ($R/R_{\odot}$)	$\log g$	Luminosity $L/L_{\odot}$	Density $\rho/\rho_{\odot}$	TESS mag	ν_f (d^{-1})	$\nu(A_{\rm max})$ (d^{-1})	$\nu_{\rm max}$ (d^{-1})	$\Delta\nu$ (d^{-1})
81003	11	221.3852	-26.9428	7428 ± 202	1.70 ± 0.29	1.48 ± 0.06	4.33 ± 0.08	6.03 ± 0.54	0.522 ± 0.109	7.79	21.17	21.17	42.42	7.31
148933	11	223.4908	-26.7326	7428 ± 193	1.87 ± 0.30	1.77 ± 0.06	4.22 ± 0.08	10.69 ± 0.83	0.340 ± 0.069	7.79	—	45.01	39.49	5.90
589826	5	71.6073	-28.0874	7943 ± 124	1.91 ± 0.30	1.57 ± 0.04	4.33 ± 0.07	8.84 ± 0.16	0.494 ± 0.091	6.02	—	48.13	44.84	6.55
975071	8	136.2965	-4.2887	7832 ± 129	1.86 ± 0.29	2.09 ± 0.06	4.07 ± 0.08	14.77 ± 0.53	0.205 ± 0.042	8.56	12.79	22.55	24.02	4.98
1404122	8	140.2844	-16.2399	8721 ± 136	2.19 ± 0.32	1.64 ± 0.05	4.35 ± 0.07	14.08 ± 0.77	0.493 ± 0.089	8.68	—	56.51	55.30	7.07
1450658	5	75.1013	-31.8133	7943 ± 128	1.91 ± 0.30	1.46 ± 0.04	4.39 ± 0.08	7.69 ± 0.20	0.608 ± 0.113	7.96	—	45.45	48.64	7.17
5165416	8, 9	142.3168	-38.4035	7492 ± 140	1.72 ± 0.28	1.87 ± 0.07	4.13 ± 0.08	9.98 ± 0.29	0.261 ± 0.056	5.94	—	16.85	24.97	4.81
5456605	7	107.8483	-0.3020	7104 ± 134	1.58 ± 0.27	4.08 ± 0.17	3.42 ± 0.09	38.14 ± 1.78	0.023 ± 0.007	5.14	—	11.15	10.20	1.48
5586741	7	111.4952	-8.6047	7764 ± 135	1.84 ± 0.29	1.64 ± 0.05	4.27 ± 0.08	8.84 ± 0.34	0.413 ± 0.0774	9.05	—	46.83	43.46	6.47
7245720	3	33.1962	-44.4890	7212 ± 136	1.62 ± 0.28	3.16 ± 0.12	3.65 ± 0.09	24.36 ± 1.10	0.051 ± 0.011	7.53	7.95	14.00	13.13	2.44
7808834	4, 5	67.7224	-41.1744	7144 ± 136	1.59 ± 0.27	3.56 ± 0.16	3.54 ± 0.09	29.74 ± 1.34	0.035 ± 0.007	6.49	6.66	6.48	10.80	2.14
9591460	10	193.5049	-25.7537	7517 ± 139	1.74 ± 0.29	1.56 ± 0.05	4.29 ± 0.08	6.98 ± 0.30	0.460 ± 0.089	8.38	19.87	42.15	41.54	6.24
10838265	3	21.0114	-8.0077	7557 ± 114	1.75 ± 0.28	1.96 ± 0.06	4.10 ± 0.08	11.33 ± 0.33	0.231 ± 0.052	6.00	14.60	30.84	23.59	4.55
10988057	14,15	303.6338	36.8066	7918 ± 128	1.90 ± 0.31	1.94 ± 0.05	4.14 ± 0.08	13.33 ± 0.34	0.260 ± 0.050	4.79	—	37.41	34.91	4.82
11199304	6	84.5453	-1.0503	8670 ± 267	2.17 ± 0.33	1.77 ± 0.06	4.28 ± 0.07	16.01 ± 1.93	0.389 ± 0.070	9.72	—	38.71	40.61	5.96
12524129	4	51.4871	-7.1214	7959 ± 128	1.91 ± 0.30	2.07 ± 0.07	4.09 ± 0.08	15.44 ± 0.69	0.216 ± 0.049	9.05	13.65	27.22	25.06	4.74
12529960	4	51.6614	-9.3663	7377 ± 128	1.68 ± 0.27	1.62 ± 0.06	4.24 ± 0.08	7.03 ± 0.41	0.393 ± 0.079	9.81	18.58	32.40	27.65	5.69
12784216	2	337.3906	-16.8090	7208 ± 122	1.62 ± 0.27	2.34 ± 0.09	3.91 ± 0.09	13.35 ± 0.65	0.126 ± 0.023	8.93	12.27	20.30	26.78	4.04
14773776	22	177.7300	12.2792	7374 ± 128	1.68 ± 0.30	1.62 ± 0.06	4.24 ± 0.09	7.00 ± 0.24	0.395 ± 0.084	6.12	—	21.08	26.87	5.73
15833513	20	100.3075	37.1022	8315 ± 164	2.05 ± 0.32	1.70 ± 0.07	4.29 ± 0.08	12.52 ± 1.01	0.414 ± 0.081	9.65	—	51.06	46.57	6.20
17466801	24,25	242.7311	32.0030	8314 ± 134	2.05 ± 0.30	1.69 ± 0.05	4.29 ± 0.07	12.33 ± 0.59	0.423 ± 0.075	7.50	—	46.66	45.19	6.40
17992601	22	170.9719	37.2348	7518 ± 128	1.74 ± 0.27	3.29 ± 0.11	3.64 ± 0.08	31.19 ± 1.18	0.049 ± 0.010	6.69	—	14.77	18.14	2.06
18658256	8,9	137.7702	-34.7247	7373 ± 131	1.68 ± 0.27	1.90 ± 0.07	4.11 ± 0.08	9.63 ± 0.43	0.244 ± 0.049	8.56	15.90	15.90	21.00	5.18
20296416	5, 6	90.8373	-38.8780	7538 ± 148	1.74 ± 0.28	1.87 ± 0.07	4.14 ± 0.08	10.16 ± 0.44	0.267 ± 0.051	8.82	16.16	24.80	27.04	4.72
20297048	5, 6	90.7633	-37.5470	7774 ± 128	1.84 ± 0.29	1.70 ± 0.05	4.24 ± 0.08	9.49 ± 0.19	0.376 ± 0.071	6.69	17.28	17.28	27.56	6.21
22211065	10	183.3755	-45.1745	7367 ± 133	1.68 ± 0.28	1.62 ± 0.06	4.24 ± 0.08	6.99 ± 0.33	0.393 ± 0.084	8.85	—	33.70	29.20	6.13
22234795	9	149.2250	-27.4751	7745 ± 128	1.83 ± 0.29	4.02 ± 0.13	3.49 ± 0.08	52.45 ± 1.95	0.028 ± 0.006	6.14	—	17.71	17.97	1.50
22525919	17	2.8986	33.6803	7918 ± 129	1.90 ± 0.30	1.66 ± 0.05	4.28 ± 0.08	9.78 ± 0.32	0.414 ± 0.079	8.51	—	44.15	38.28	5.69
22749863	18	38.4222	27.3721	8354 ± 165	2.06 ± 0.31	1.60 ± 0.05	4.35 ± 0.07	11.19 ± 0.70	0.507 ± 0.091	8.84	—	41.90	47.17	6.21
23137953	4	46.0564	-8.4645	7412 ± 151	1.69 ± 0.30	2.16 ± 0.08	4.00 ± 0.09	12.70 ± 0.71	0.168 ± 0.033	8.00	12.27	22.90	19.44	4.71
23555158	9, 10	168.9978	-32.3701	7427 ± 138	1.70 ± 0.29	1.71 ± 0.06	4.20 ± 0.08	8.05 ± 0.36	0.338 ± 0.062	8.33	—	33.70	33.44	5.76
24344701	5	79.0020	-9.8098	8270 ± 146	2.03 ± 0.30	1.56 ± 0.05	4.36 ± 0.08	10.20 ± 0.64	0.539 ± 0.099	9.74	—	72.58	75.17	7.27
24523461	5	80.3114	-7.4800	8290 ± 186	2.04 ± 0.31	1.63 ± 0.05	4.32 ± 0.07	11.31 ± 0.81	0.471 ± 0.098	8.05	—	35.42	41.99	6.26
25195864	4-6	63.7537	-69.5367	7523 ± 112	1.74 ± 0.27	3.00 ± 0.12	3.72 ± 0.08	26.04 ± 1.39	0.064 ± 0.016	10.46	—	26.78	20.74	2.70
26074369	8	151.0802	-9.1616	7225 ± 139	1.62 ± 0.26	3.06 ± 0.12	3.68 ± 0.08	22.92 ± 1.29	0.057 ± 0.012	8.29	—	16.42	13.82	2.64
26174577	8	152.5088	-10.8622	7416 ± 124	1.70 ± 0.29	1.55 ± 0.06	4.29 ± 0.08	6.55 ± 0.29	0.455 ± 0.086	9.13	—	26.96	23.67	6.82
26500322	18	57.0771	29.9475	8782 ± 171	2.21 ± 0.32	2.72 ± 0.17	3.91 ± 0.08	39.50 ± 5.45	0.110 ± 0.026	9.08	—	39.74	42.42	2.85
26633024	24	355.2381	51.3192	8136 ± 137	1.98 ± 0.31	1.63 ± 0.05	4.31 ± 0.08	10.51 ± 0.56	0.456 ± 0.088	10.07	—	54.86	48.04	6.68
26749728	14, 15	292.9083	48.4425	8200 ± 145	2.01 ± 0.30	1.60 ± 0.06	4.33 ± 0.08	10.47 ± 0.45	0.487 ± 0.093	8.66	—	56.85	54.17	6.97
26957587	21	149.5299	22.6643	7728 ± 127	1.82 ± 0.29	2.03 ± 0.06	4.08 ± 0.08	13.25 ± 0.47	0.217 ± 0.042	8.07	11.40	11.40	29.81	4.92
28679106	14	282.8152	33.3234	8094 ± 146	1.97 ± 0.31	1.60 ± 0.05	4.33 ± 0.08	9.84 ± 0.55	0.485 ± 0.094	9.58	—	61.17	52.96	7.05
29862383	3	24.2247	-17.2810	8340 ± 127	2.06 ± 0.30	1.87 ± 0.08	4.21 ± 0.08	15.20 ± 1.14	0.316 ± 0.066	9.62	—	40.09	35.86	5.36
30624832	14	289.6779	31.6878	7517 ± 161	1.74 ± 0.29	1.54 ± 0.06	4.31 ± 0.08	6.79 ± 0.35	0.479 ± 0.089	8.12	20.24	38.45	32.92	5.94
31475829	5, 6	84.0430	-28.7080	8127 ± 126	1.98 ± 0.29	1.49 ± 0.05	4.39 ± 0.07	8.73 ± 0.32	0.598 ± 0.103	6.13	—	59.62	56.42	7.42
31870361	1,3,7,10	53.1931	-66.7294	7141 ± 139	1.59 ± 0.27	3.69 ± 0.15	3.51 ± 0.08	31.86 ± 1.56	0.032 ± 0.007	7.18	—	10.80	12.53	1.78
32559046	5,6	84.9333	-25.6212	8156 ± 124	1.99 ± 0.31	1.54 ± 0.05	4.36 ± 0.07	9.45 ± 0.41	0.546 ± 0.101	9.04	—	50.98	50.72	7.02
32763133	6	86.4687	-29.0921	8422 ± 138	2.09 ± 0.31	1.62 ± 0.05	4.34 ± 0.07	11.87 ± 0.62	0.493 ± 0.089	8.84	—	57.11	53.05	7.26
34197596	5	61.0076	-11.7484	8618 ± 129	2.15 ± 0.30	1.51 ± 0.04	4.41 ± 0.07	11.28 ± 0.59	0.629 ± 0.111	8.63	—	62.90	58.84	6.74
34308379	5	62.2324	-9.6240	8567 ± 131	2.14 ± 0.31	1.64 ± 0.06	4.34 ± 0.07	13.05 ± 0.78	0.485 ± 0.092	9.76	—	54.69	52.96	6.77
34737955	6	95.9950	-13.2070	7282 ± 158	1.64 ± 0.28	1.62 ± 0.06	4.23 ± 0.08	6.65 ± 0.46	0.386 ± 0.084	9.16	18.14	18.14	28.25	6.00